



Analysis of the confinement string in (2+1)-dimensional Quantum Electrodynamics with a trapped-ion quantum computer



Arianna Crippa ^{1,2} , Karl Jansen ^{1,3} & Enrico Rinaldi ^{4,5,6,7}

Understanding strongly interacting quantum field theories is a central challenge in theoretical physics, with direct relevance to nuclear, high-energy and condensed matter systems. Here we present a quantum algorithm for compact lattice Quantum Electrodynamics in 2+1 dimensions with dynamical fermionic matter. Using a variational quantum approach, we extract the static potential between charges across Coulomb, confinement, and string-breaking regimes. Our method employs a symmetry-preserving, resource-efficient circuit to prepare ground states, enabling accurate calculations on the Quantinuum H1-1 trapped-ion device and emulator, in agreement with noiseless simulations. Moreover, we visualize the electric field flux configurations that mainly contribute to the wave function of the quantum ground state, giving insights into the mechanisms of confinement and string-breaking. These results are a promising step forward in the grand challenge of solving higher dimensional lattice gauge theory problems with quantum computing algorithms.

One of the most prominent examples of non-perturbative physics is the confinement of constituent particles in gauge theories. In fact, this has been one of the main motivations for Wilson to introduce lattice gauge theories (LGTs)^{1–3}. In Quantum Chromodynamics (QCD)⁴ the confinement phenomenon is responsible for the binding of quarks and gluons into hadrons at low energies (large distances). Confinement between static charges also plays a vital role in Quantum Electrodynamics (QED) in (2 + 1) dimensions, where it is related to the physics of instantons^{5,6}.

A very interesting situation arises when a confining gauge theory is coupled to matter fields. When the energy of the confining string becomes too large, it is energetically more favorable to form heavy-light meson states between a static charge and a particle excitation from the dynamical matter field. This is the celebrated phenomenon of *string breaking* and it has been studied in LGT with Monte Carlo (MC) from the pioneering work of refs. 7,8. See the review ref. 9 of LGT studies of string breaking in the action formulation.

To be more concrete, in (2 + 1) dimensions the QED static potential between two static charges at distance r has a Coulomb logarithmic term, a

confining linear part and a string breaking regime^{10,11}:

$$V(r) = V_0 + \alpha \log r + \sigma r, \quad (1)$$

where α is the coupling, σ the *string tension* and V_0 refers to a constant term. The form of the static potential is illustrated in Fig. 1a.

At small r , $V(r)$ is a logarithmic function representing the Coulomb potential in two space dimensions. The coupling which determines the strength of the Coulomb potential becomes perturbative with decreasing distance, due to asymptotic freedom. At intermediate distances, the electric field between a pair of static charges forms a flux tube (or string) between them, leading to a linear behavior of the potential as a function of the distance and hence to confinement of the static charges. However, when dynamical matter fields are included, the linear potential does not extend to indefinitely large distances. For sufficiently large separations it is energetically favorable to pair-produce a particle and antiparticle with opposite charges, thereby *breaking* the string. The static charges are screened by the dynamical matter fields and now bound in heavy-light mesons.

¹Deutsches Elektronen-Synchrotron DESY, Platanenallee 6, 15738 Zeuthen, Germany. ²Institut für Physik, Humboldt-Universität zu Berlin, Newtonstr. 15, 12489 Berlin, Germany. ³Computation-Based Science and Technology Research Center, The Cyprus Institute, 20 Kavafi Street, 2121 Nicosia, Cyprus. ⁴Quantinuum K.K., Financial City Grand Cube 3F, 1-9-2 Otemachi, Chiyoda-ku, Tokyo, Japan. ⁵Interdisciplinary Theoretical and Mathematical Sciences (iTHEMS) Program, RIKEN, Wako, Saitama, 351-0198, Japan. ⁶Center for Quantum Computing (RQC), RIKEN, Wako, Saitama, 351-0198, Japan. ⁷Theoretical Quantum Physics Laboratory, Cluster of Pioneering Research, RIKEN, Wako, Saitama, 351-0198, Japan. e-mail: arianna.crippa@desy.de

With the advent of quantum technologies, and quantum computing in particular, the study of confinement, and in general lattice gauge theories, has become one of the exciting areas of discovery and development. In recent years, lower dimensional LGTs are helping to explore the potential of applying quantum computing to high energy physics, to develop quantum algorithms and are opening new ways of computations to tackle physical problems, see the reviews^{12–15}. For example, the phenomenon of string breaking has been considered in the context of quantum simulators^{16–18}, using tensor networks^{19–21} and, more recently using quantum hardware^{21–23}.

While the focus in these latter papers is more on the dynamics of the string in some specific LGTs, in our work we will study static flux configurations in the different regimes of the static potential as well as the probability of the states contributing at different bare gauge couplings. Moreover, to the best of our knowledge, our work is the first one addressing the static potential of QED in (2 + 1) dimensions by preparing the ground state of the QED Hamiltonian at multiple couplings across a variety of distances.

In this work, we perform a qualitative analysis of the static potential, in the regimes described above, by considering QED in (2 + 1) dimensions and a quantum computing approach with ion-trap devices. In Fig. 1a we define the static potential as a function of the distance $r = a \cdot r_{\text{lat}}$, i.e. is the product of the lattice spacing a and the lattice Euclidean distance r_{lat} between the two sites on the lattice where static charges are placed. Increasing the physical distance at a fixed lattice spacing requires placing the static charges at lattice sites that are farther apart: this is possible only with a very large number of lattice sites, which is too costly to simulate or implement on a quantum computer. We consider two static charges at a fixed distance r_{lat} in lattice units and vary the lattice spacing, therefore changing r . Due to the non-perturbative nature of the quantum field theory, the lattice spacing is controlled by the coupling constant g , introduced in the Hamiltonian, Eq. (2). In other words, the lattice spacing is an implicit function of the coupling, varying g will then change the lattice spacing, and hence the physical distance r . This enables us to conduct an analysis and study confinement and string-breaking phenomena with limited resources. The implicit function $a(g)$ is not known a priori, and its precise form is not relevant to our study. The three regimes of interest can be distinguished by examining the potential energy as a function of g .

One advantage we want to point out is our ability to visualize the electric fluxes appearing in the ground state and thus obtain direct information about the flux configurations in the different regimes of the static potential. We observe this phenomenon experimentally on the quantum computer H-series System Model H1-1 at Quantinuum²⁴. This not only allows to achieve new insights in the physics of the considered model but also sets the basis for future quantum analyses on this interesting topic and also shows the precision of the results with ion-trapped devices. Another advantage we see in our application is the possibility to place static charges on the lattice by hand and only need to compute the ground state to determine the static potential.

Results

QED Hamiltonian

In this work, we consider a lattice discretization of (2 + 1)-d QED using Kogut–Susskind staggered fermions^{25–27}. This formulation has been introduced in order to deal with the so-called *doubling problem*^{2,28,29}, i.e. an incorrect continuum limit of the theory, that arises with a naive lattice discretization of the fermionic degrees of freedom.

The spinor components are distributed on different lattice sites, thus excluding the additional (unphysical) degrees of freedom. In Fig. 1b we depict the basic components that build the lattice structure for (2 + 1)-dimensional QED. In particular, we describe how the gauge and fermionic degrees of freedom are represented on the lattice. The fermions put onto the sites (*dashed circles* describe matter fields, *solid circles* antimatter fields), while gauge fields are the links connecting the sites (*arrows*). The Hamiltonian can be written as,

$$\hat{H}_{\text{QED}} = \frac{g^2}{2} \sum_{\mathbf{n}} \left(\hat{E}_{\mathbf{n},x}^2 + \hat{E}_{\mathbf{n},y}^2 \right) \quad (2a)$$

$$- \frac{1}{2a^2 g^2} \sum_{\mathbf{n}} \left(\hat{P}_{\mathbf{n}} + \hat{P}_{\mathbf{n}}^\dagger \right) \quad (2b)$$

$$+ m \sum_{\mathbf{n}} (-1)^{n_x+n_y} \hat{\phi}_{\mathbf{n}}^\dagger \hat{\phi}_{\mathbf{n}} \quad (2c)$$

$$+ \frac{i}{2a} \sum_{\mathbf{n}} \left(\hat{\phi}_{\mathbf{n}}^\dagger \hat{U}_{\mathbf{n},x}^\dagger \hat{\phi}_{\mathbf{n}+x} - \text{h.c.} \right) \quad (2d)$$

$$- \frac{1}{2a} \sum_{\mathbf{n}} (-1)^{n_x+n_y} \left(\hat{\phi}_{\mathbf{n}}^\dagger \hat{U}_{\mathbf{n},y}^\dagger \hat{\phi}_{\mathbf{n}+y} + \text{h.c.} \right).$$

The electric energy in Eq. (2a), is built with $\hat{E}_{\mathbf{n},\mu}$, the dimensionless electric field operator that acts on the link with initial coordinates $\mathbf{n} = (n_x, n_y)$ and direction $\mu \in \{x, y\}$. The bare coupling g , is also present in the magnetic term, Eq. (2b). Here, the *plaquette operator* $\hat{P}_{\mathbf{n}} = \hat{U}_{\mathbf{n},y} \hat{U}_{\mathbf{n}+y,x} \hat{U}_{\mathbf{n}+x,y}^\dagger \hat{U}_{\mathbf{n},x}^\dagger$, Fig. 1c, defines the strength of the interaction (with the notation $\mathbf{n} + x \equiv (n_x + 1, n_y)$ or $\mathbf{n} + y \equiv (n_x, n_y + 1)$). The unitary link operators $\hat{U}_{\mathbf{n},\mu}$ represent the gauge connection between the fermionic fields and are related to the discretized vector field $\hat{A}_{\mathbf{n},\mu}$ as

$$\hat{U}_{\mathbf{n},\mu} = e^{iag\hat{A}_{\mathbf{n},\mu}}, \quad (3)$$

where $ag\hat{A}_{\mathbf{n},\mu}$ is restricted to $[0, 2\pi)$, thus the group of gauge transformations is the compact $U(1)$ group. In the following, the coupling g will be defined as a function of the *lattice spacing*, $g \mapsto g(a)$. We then set $a = 1$ without loss of generality.

The electric field $\hat{E}_{\mathbf{n},\nu}$ and the link operator $\hat{U}_{\mathbf{n}',\mu}$ are connected through the commutation relations,

$$[\hat{E}_{\mathbf{n},\nu}, \hat{U}_{\mathbf{n}',\mu}] = \delta_{\mathbf{n},\mathbf{n}'} \delta_{\nu,\mu} \hat{U}_{\mathbf{n},\nu}, \quad (4)$$

$$[\hat{E}_{\mathbf{n},\nu}, \hat{U}_{\mathbf{n}',\mu}^\dagger] = -\delta_{\mathbf{n},\mathbf{n}'} \delta_{\nu,\mu} \hat{U}_{\mathbf{n}',\nu}^\dagger. \quad (5)$$

The last two terms in the Hamiltonian describe the fermionic degrees of freedom. Starting from a continuum formulation with two-component Dirac spinors, we discretize the Hamiltonian with the staggered formulation. The fermionic mass term, involving the bare lattice fermion mass m , Eq. (2c), has a single-component fermionic field ($\hat{\phi}_{\mathbf{n}}$) residing on the site \mathbf{n} . We have carried out an analysis with different masses and selected a value ($m = 2$) that clearly shows the different regimes of the static potential, as illustrated in Fig. 1a. The kinetic term, in Eq. (2d), describes a process in which a fermion moves between two neighboring lattice sites, causing an associated alteration of the electric field along the link connecting these sites.

The states that fulfill Gauss’s law at each site \mathbf{n} , Fig. 1d,

$$\left[\sum_{\mu=x,y} \left(\hat{E}_{\mathbf{n}-\mu,\mu} - \hat{E}_{\mathbf{n},\mu} \right) - \hat{q}_{\mathbf{n}} - Q_{\mathbf{n}} \right] |\Phi\rangle = 0 \quad (6)$$

$$\iff |\Phi\rangle \in \mathcal{H}_{\text{ph}},$$

belong to a gauge invariant subspace \mathcal{H}_{ph} . In this equation,

$$\hat{q}_{\mathbf{n}} = \hat{\phi}_{\mathbf{n}}^\dagger \hat{\phi}_{\mathbf{n}} - \frac{1}{2} [1 + (-1)^{n_x+n_y+1}] \quad (7)$$

are *dynamical charges*, and $Q_{\mathbf{n}}$ represent *static charges*.

In this work, we impose Gauss’s law and study only the physically relevant subspace. By applying this method, we reduce the number of links to a subset of dynamical ones, i.e. we can rewrite some of them in terms of a reduced set of independent variables, by solving Eq. (6).

In “Supplementary Note 3: Truncation and Gauss’s law dependence” we analyze how the difference is strictly connected to the truncation used, becoming negligible when considering large l . This effect is more

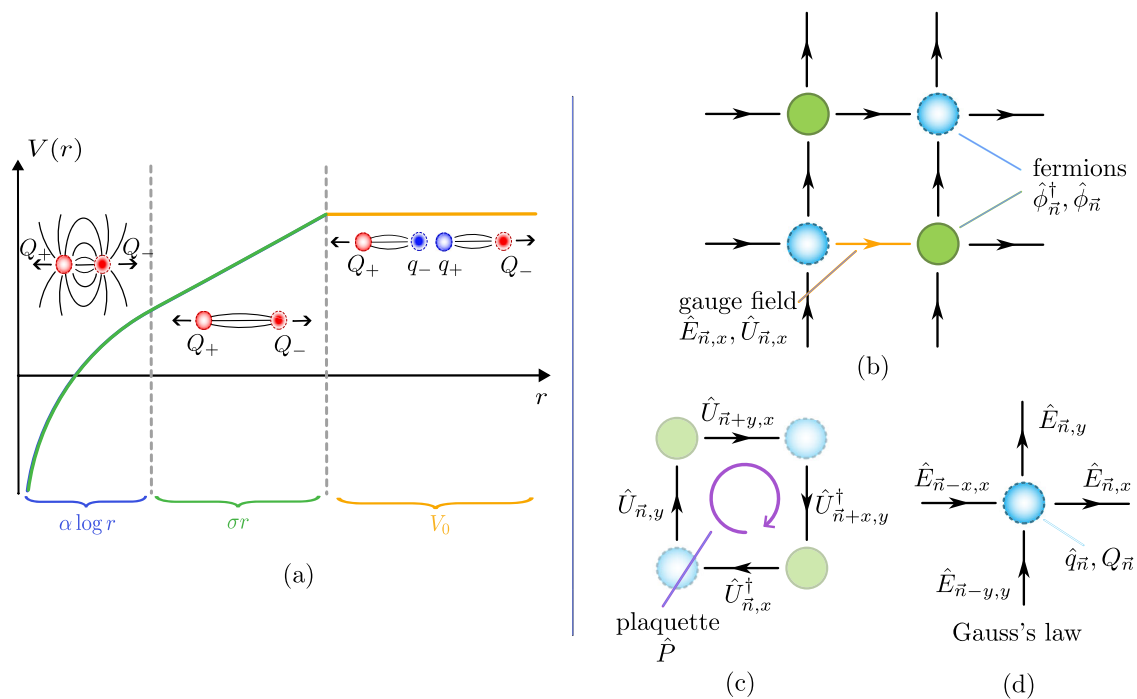


Fig. 1 | Static potential of two charges and lattice structure for (2 + 1)-dimensional QED. **a** The expected behavior of the static potential $V(r)$ for this model as a function of the distance of two static charges, r . For small r (blue section) there is a Coulomb potential. Then, an electric flux tube forms between the charges when the distance increases (green section) dominating the potential in this regime. At a certain r the flux tube breaks and a new pair of charge/anticharge forms (orange section), and hence the linear part of the potential is not continuing. This is the

qualitative non-perturbative picture of the transition between confinement and charge screening in QED with light matter fields, and it is similar to the one in QCD in (3 + 1) dimensions. **b** The gauge fields live on the links which connect the fermionic sites on the lattice. **c** The plaquette operator is the product of four link operators $\hat{P}_{\mathbf{n}} = \hat{U}_{\mathbf{n},y} \hat{U}_{\mathbf{n}+y,x} \hat{U}_{\mathbf{n}+x,y}^\dagger \hat{U}_{\mathbf{n},x}^\dagger$. **d** Gauss's law for the fermionic site \mathbf{n} controls the balance between ingoing/outgoing electric field and dynamical charge $\hat{q}_{\mathbf{n}}$ (and eventual static charge $Q_{\mathbf{n}}$), Eq. (6).

pronounced also for small values of the bare coupling g . At larger $g \gtrsim 1.0$, the electric flux and string breaking results with $l = 1$ are compatible with larger truncations. Since the choice of dynamical links does not affect the electric flux configurations and the string breaking phenomenon, they can be studied qualitatively at small truncations.

In general, the number of dynamical links, before Gauss's law has been applied follows the rule $\ell = n \sum_{i=1}^d \frac{(n_i-1)}{n_i}$ ($\ell = nd$) total number of links in OBC (PBC) system, with $n = n_1 \times n_2 \dots \times n_d$ number of sites, $d =$ spatial dimensions. With $n - 1$ constraint from Gauss's law, we have a total of $\tilde{\ell} = \ell - (n - 1)$ dynamical links, e.g. a 3×2 OBC system has a subset of $\tilde{\ell} = 6[(3 - 1)/3 + (2 - 1)/2] - (6 - 1) = 2$ dynamical links, while a 4×3 OBC system has $\tilde{\ell} = 12[(4 - 1)/4 + (3 - 1)/3] - (12 - 1) = 6$. After the Gauss's law has been applied, there is no residual constraint left.

Numerical implementation of gauge fields. We have seen that the compact $U(1)$ group describes QED. However, for a numerical implementation of the Hamiltonian on finite computational resources, we need to consider a correspondingly finite set of possible solutions: this is achieved with a truncation of the infinite-dimensional gauge Hilbert space. Here, we follow the truncation of $U(1)$, in the electric basis, to \mathbb{Z}_{2l+1} , where l defines the truncation and sets the Hilbert space dimension³⁰. With this method, the unbounded gauge degrees of freedom are truncated to a finite dimension within the range $[-l, l]$, resulting in a total Hilbert space dimension of $(2l+1)^N$, where N denotes the number of gauge fields in the system. After the truncation, the eigenstates of the electric field operator, $\hat{E}_{\mathbf{n},\mu}$, form a basis for the link degrees of freedom. From Eqs. (4) and (5), the link operators $\hat{U}_{\mathbf{n},\mu}$ ($\hat{U}_{\mathbf{n},\mu}^\dagger$) act as a raising (lowering) operator on the electric field eigenstates,

$$\hat{E}_{\mathbf{n},\mu} |e_{\mathbf{n},\mu}\rangle = e_{\mathbf{n},\mu} |e_{\mathbf{n},\mu}\rangle, \text{ with } e_{\mathbf{n},\mu} \in [-l, l], \quad (8)$$

$$\hat{U}_{\mathbf{n},\mu} |e_{\mathbf{n},\mu}\rangle = |e_{\mathbf{n},\mu} + 1\rangle, \quad \hat{U}_{\mathbf{n},\mu}^\dagger |e_{\mathbf{n},\mu}\rangle = |e_{\mathbf{n},\mu} - 1\rangle. \quad (9)$$

Alternative ways to provide a suitable formulation for a numerical analysis can be done with quantum link models, with a cyclic group, or also encoding the gauge fields with qudits^{17,31-35}.

3 × 2 lattice

In this work, we fix the position of two static charges on the lattice, at a fixed distance of $r = \sqrt{5}$, and vary the bare coupling g . The first lattice system studied is depicted in Fig. 2a. The total number of qubits for the quantum circuit is 10 (4 for the gauge fields with truncation $l = 1$ and 6 for the fermions) and we employed the mutual information to construct the entanglement structure between the qubits, “Supplementary Note 1: Quantum circuit definition”.

Table 1 shows the resource estimation for this system size and three values of the truncation, $l = 1, 3, 7$. In particular, we show the total number of qubits used, the number of variational parameters, CNOT gates and their depth, which refers to the amount of CNOT layers. Every layer is represented by parallel CNOTs in the quantum circuit, e.g. if a first CNOT acts on qubit q_1 and q_2 and a second CNOT gate on q_3 and q_4 , they belong to the same layer. Two different layers are counted if the second gate acts also on q_1 or q_2 .

We first consider a noiseless analysis with the Variational Quantum Eigensolver (VQE)³⁶. The top panel of Fig. 2b shows the comparison between the static potential $V(r)$ with exact diagonalization (ED) (solid line) and the quantum variational results (triangles), performed with the Nakanishi–Fujii–Todo (NFT) optimizer^{37,38} and 10^4 shots. This optimizer constructs an analytical expression for the energy expectation given that the energy expectation as a function of a single parameter can be expressed using a sine function. Requiring three independent energy evaluations, it

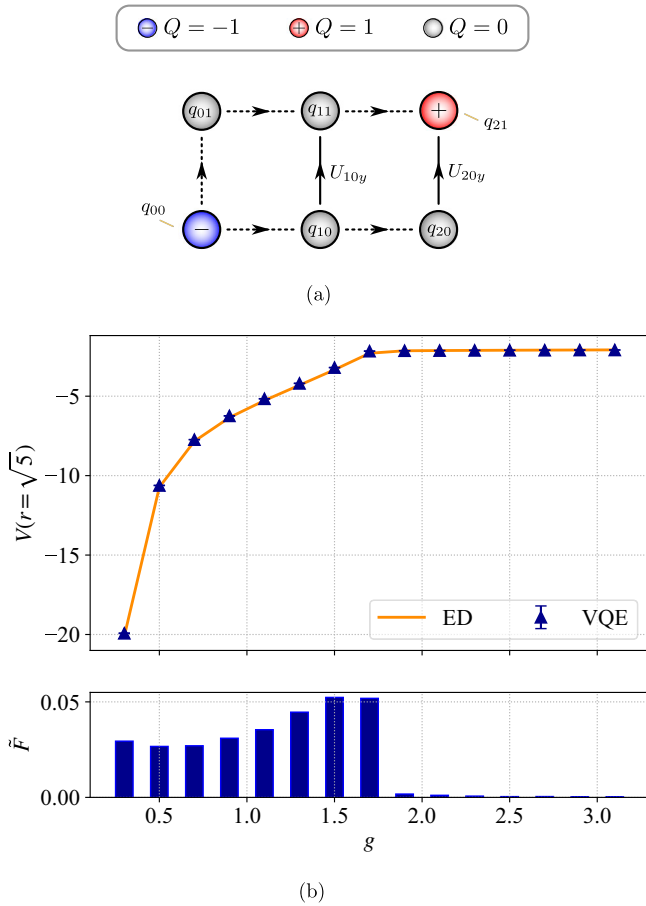


Fig. 2 | Lattice system 3 × 2 and variational quantum results (noiseless simulator). **a** Two static charges with values $Q \pm 1$ are placed onto two sites $\mathbf{n} = (n_x, n_y)$: $Q = -1 \mapsto (0, 0)$, $Q = 1 \mapsto (2, 1)$. The symbols q_n are the values of the dynamical charges onto the sites with coordinates $n = n_x n_y$. The dashed arrows are the inactive gauge links after Gauss’s law is applied, solid arrows represent the link operators that remain dynamical, U_{10y} , U_{20y} . The quantum circuit (“Supplementary Note 1: Quantum circuit definition”) describes these links and the fermionic charges q_n (top **b**) Static potential at different coupling g with ED (solid line) and quantum variational results (triangles), performed with Nakanishi–Fujii–Todo (NFT) optimizer and 10^4 shots. (bottom **b**) Infidelity ($1 - \text{fidelity}$) between variational quantum data and Exact Diagonalization (ED). A finite number of shots defines the error bars, which are smaller than the markers.

Table 1 | Resources required for the variational circuit for Gray encoding at different gauge fields truncation l

Resource estimation 3 × 2 OBC system				
l	# Qubits	# CNOTs	CNOT Depth	# Parameters
1	10	152	60	30
3	12	200	88	41
7	14	252	122	54

In a 3 × 2 Open Boundary Conditions (OBC) system with fermions, the two dynamical gauge fields and fermionic sites can be simulated with the specified total number of qubits. In particular, the number of qubits for the fermions is fixed to 6. Additionally, we quantify the total count of CNOT gates and the CNOT depth, representing the layers of CNOT gates in the circuit. The rightmost column displays the total number of parameters in the variational Ansatz.

eliminates the need for computing gradients. In the bottom panel, we show the infidelity of the results,

$$\tilde{F} \equiv 1 - F = 1 - |\langle \psi_{\text{VQE}} || \psi_{\text{ED}} \rangle|^2, \tag{10}$$

where F is the fidelity. We see that the infidelity \tilde{F} is $<5\%$ at almost every coupling g considered, and we are able to reproduce the expected behavior of the static potential with our variational ground state Ansatz. For the analysis, we consider optimization results coming from two different and independent initial points in parameter space:

- We consider a set of initial parameters that correspond to the preparation of the vacuum state and the electric strings. Then we perturb them with additive Gaussian noise before starting the optimization. This ensures that we have a large probability of reaching configurations corresponding to the vacuum and an electric flux tube.
- Alternatively, we consider parameters corresponding to the preparation of the string breaking configuration. We add an additive Gaussian noise perturbation and then start the optimization procedure. It is possible to define both the initial states above by directly inspecting the lattice structure and the encoding utilized in this project. The results from both initial points are compared and we select the set of optimized parameters that gives the state with the highest fidelity, which usually depends on the value of the coupling constant g . If the fidelity cannot be computed, there are protocols to test for convergence of the variational optimization and to decide which variational parameters to use³⁰.

The uncertainties (standard deviation) are computed with the combination of the variances of the Pauli terms P_i in the Hamiltonian, which is a sum of Pauli strings, $\hat{H} = \sum_i c_i P_i$, (with c_i coefficients)³⁹. The expectation value of \hat{H} can be written as

$$\langle \psi | \hat{H} | \psi \rangle = \sum_i c_i \langle \psi | P_i | \psi \rangle. \tag{11}$$

If we perform n times of measurements (shots) for each Pauli string P_i , the variance of the estimated $\langle \psi | P_i | \psi \rangle$ due to a finite n is

$$\sigma_{P_i}^2 = \langle \psi | P_i^2 | \psi \rangle - \langle \psi | P_i | \psi \rangle^2 = 1 - \langle \psi | P_i | \psi \rangle^2. \tag{12}$$

Then, the final standard deviation error is

$$\sigma = \sqrt{\sum_i |c_i|^2 \frac{1 - \langle \psi | P_i | \psi \rangle^2}{n}}. \tag{13}$$

Sampling in the computational basis. We select three values of the coupling representing the main regimes in the static potential: Coulomb, linear electric strings and string breaking with $g = 0.3, 1.1, 1.9$, respectively. With the optimal parameters obtained from the solutions of the quantum variational approach, we build the quantum circuit to prepare the ground state and we run it on the emulator H1-1E and on the real quantum hardware H1-1, see Section “Methods” for details on the hardware. Note that before running on these devices, the circuits are rebased to the native operations of the H-series machines and are optimized using the `pytket` default optimization. This results in a two-qubit gate count of $\sim 80 R_{zz}$ arbitrary angle operations, a significant reduction compared to the resources of Table 1.

We sample the final state of the circuit and show the configurations with the highest probability in Figs. 3a, b and 5. On the x -axis, the states $|\psi_f\rangle \otimes |\psi_g\rangle$ assume numerical values corresponding to the sampled bit-strings from measuring the quantum state in the computational basis. In all the figures, the error bars on the probability are obtained by considering the shots to be drawn from a Bernoulli distribution.

In the weak coupling regime, there are many basis states with non-negligible amplitudes, as depicted in Fig. 3a, thus the ground state is represented by a superposition of a lot of different possible configurations. The basis state with the highest probability corresponds to a vacuum configuration for both gauge fields and fermionic sites,

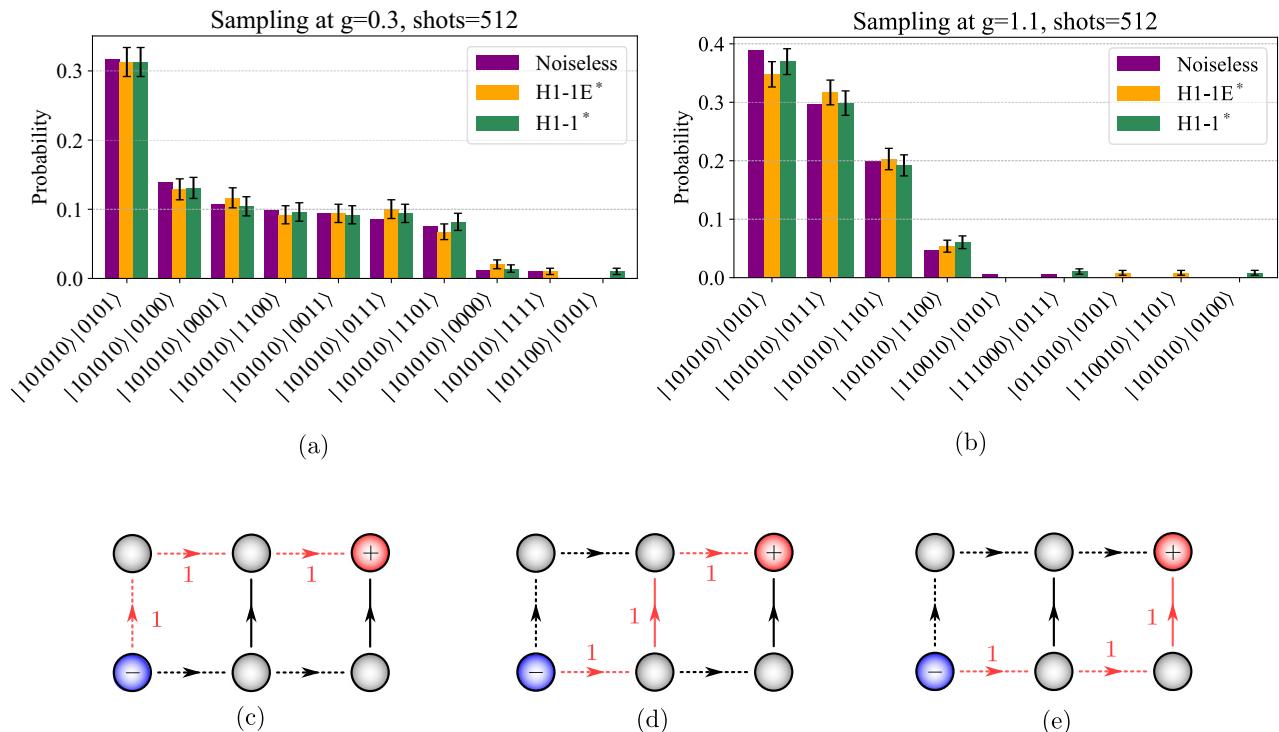


Fig. 3 | Ground state probabilities and lattice configurations at coupling $g = 0.3, 1.1$. **a** (bars from left to right) Noiseless results (state vector calculation with the optimal parameter from VQE), emulator H1-1E and real quantum hardware H1-1. The emulator and hardware results were performed in a single run with 512 shots. The data mitigated by excluding the unphysical bitstrings are indicated by (*). **b** (bars from left to right) Noiseless results (state vector calculation with the optimal parameter from VQE), emulator H1-1E and real quantum hardware H1-1. The emulator and hardware results were performed in a single run with 512 shots. The data mitigated by excluding the unphysical bitstrings are indicated by (*). For this intermediate value of g we observe that the states with the highest probability form three configurations with electric strings between the static charges. In both panels, the error bars on the probability are obtained by considering the shots to be drawn from a Bernoulli distribution. **c** Represents the configuration $|101010\rangle \otimes |0101\rangle$, i.e.

zero eigenvalues for the two dynamical gauge fields (solid arrows) and no dynamical charges on the sites, see Section “Methods” for translation rules. Static charges correspond to \pm symbols on the sites. The electric flux is depicted with red arrows with a value of ‘1’. **d** The configuration $|101010\rangle \otimes |0111\rangle$ is the case where no dynamical charges are forming onto the sites and the eigenvalues for the links $\{U_{10y}, U_{20y}\}$ are $\{1, 0\}$ respectively. An electric flux flowing through the center of the system can be seen. **e** Represents the configuration $|101010\rangle \otimes |1101\rangle$, the electric flux runs through the rightmost sites. The links and sites (values of the dynamical charges) without a number are equal to zero. Note that the difference in the probabilities of (c) and (e) is mainly attributed to the small truncation used in the analysis. We have tested this with exact diagonalization and a higher truncation $l = 7$ and found that (c) and (e) have the same probabilities.

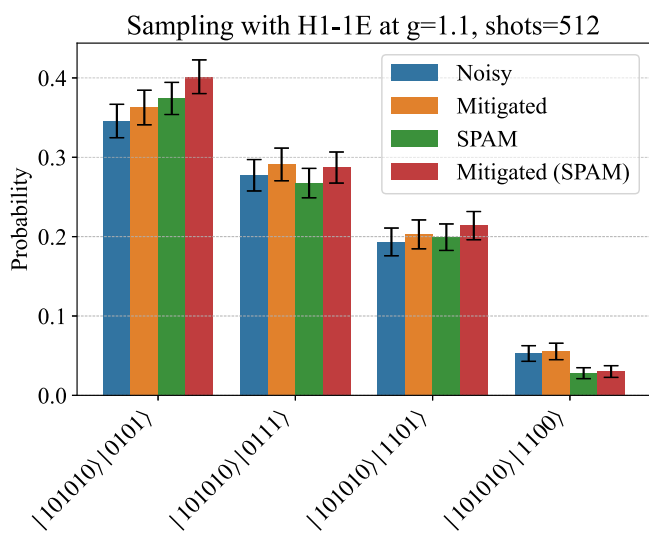


Fig. 4 | Ground state probabilities at coupling $g = 1.1$ with emulator H1-1E. (bars from left to right) Comparison between noisy results (‘Noisy’) and mitigated via the exclusion of unphysical bitstrings (‘Mitigated’). SPAM error mitigation (‘SPAM’) and subsequent bitstrings exclusion are also considered (‘Mitigated (SPAM)’). The error bars on the probability are obtained by considering the shots to be drawn from a Bernoulli distribution.

$|v\rangle = |101010\rangle \otimes |0101\rangle$, Section “Methods”. This result corresponds to Fig. 3c and depends on the choice of dynamical links during the application of Gauss’s law into the configurations on the lattice. The interpretation is discussed extensively in “Supplementary Note 3: Truncation and Gauss’s law dependence”. From the left, the bars define the noiseless results, computed with a state vector calculation with the optimal parameters from the variational quantum analysis. The bars in the center and right are the probabilities of the states obtained with the H1-1E emulator and on the real quantum hardware H1-1, respectively. The runs on Quantum devices were performed with a fixed number of shots of 2^9 .

For increasing g , the probabilities and the corresponding configurations are depicted in Fig. 3b. Here we translate the results in the plot, by applying Gauss’ law, into the configurations on the lattice. If we consider, e.g. the configuration (b) $|101010\rangle \otimes |0111\rangle$, we can see that corresponds to the case where no dynamical charges are forming onto the sites and the eigenvalues for the links $\{U_{10y}, U_{20y}\}$ are $\{1, 0\}$ respectively. If we apply these numerical values into Eq. (6), we get the lattice of Fig. 3d, with an electric flux flowing through the center of the system, thus consistent with the confinement regime identified in Fig. 2b. We also test the coupling $g = 1.1$ on H1-1E with the application of the SPAM mitigation technique, see Section “Methods” for more details. In Fig. 4, we plot the noisy results and their corresponding mitigated values from left to right by excluding the unphysical bitstrings. Then we consider a run with the SPAM method and apply the same mitigation. We can see that the results are not highly affected by the

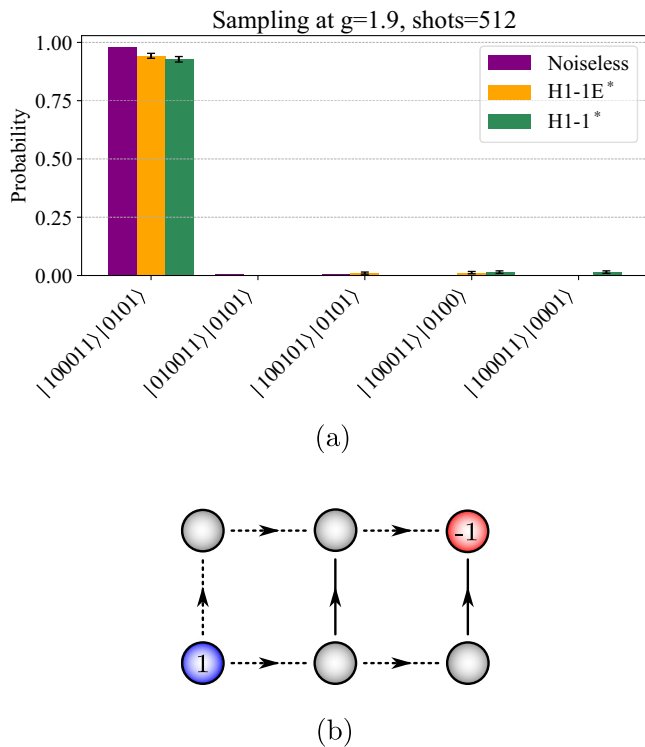


Fig. 5 | Ground state probabilities and lattice configuration at coupling $g = 1.9$. **a** (bars from left to right) Noiseless results (state vector calculation with the optimal parameter from VQE), emulator H1-1E and real quantum hardware H1-1. The emulator and hardware results were performed in a single run with 512 shots. The data mitigated by excluding the unphysical bitstrings are indicated by (\dagger). The error bars on the probability are obtained by considering the shots to be drawn from a Bernoulli distribution. **b** The most favorable configuration corresponds to the electric strings breaking with the formation of two particle/antiparticle pairs. This state refers to the lattice where links and sites without a number are equal to zero, while the values ± 1 that appear on the sites correspond to two non-zero dynamical charges \hat{q} .

SPAM mitigation and for every case they could reach the desired noiseless configurations of Fig. 3b.

At strong g we have a shift to a different regime with basically a single configuration, Fig. 5. In this case, we do not have electric strings between the static charges (as in Fig. 3b–e), but we see the formation of two dynamical charges, representing string breaking and the creation of a particle/antiparticle pair, consistent with Fig. 2b. We also compute the coupling where we see the transition between linear and string breaking regime, $g \sim 1.7$. Figure 6a illustrates again accurate results both with H1-1E and H1-1, with the most probable states as in Fig. 3c–e. This data point corresponds to a region where the energy gap, i.e. between the ground state and the first excited state, becomes small, as depicted in Fig. 6b.

Static potential results. We now consider the calculation of the static potential for five values of the bare coupling. Figure 7 shows a comparison between the data with H1-1E (emulator) and H1-1 (quantum hardware). For the couplings $g = 0.3, 0.7, 1.1, 1.5$ we used a combination of PMSV and SPAM error mitigation methods, included in the software InQuanto⁴⁰. For the last coupling $g = 1.9$ we considered a different algorithm based on sampling in the computational basis³⁹, where only the $R = 4$ most probable states are used, and we applied an error mitigation technique consisting in the post-processing of the sampled bitstrings to remove the ones with unphysical constraints.

The emulator results (triangles) have been computed with 2^{10} shots, while for the hardware runs (circles), we used 2^9 shots for each g using only a single run. The inserted plot highlights the relative error ϵ between the data

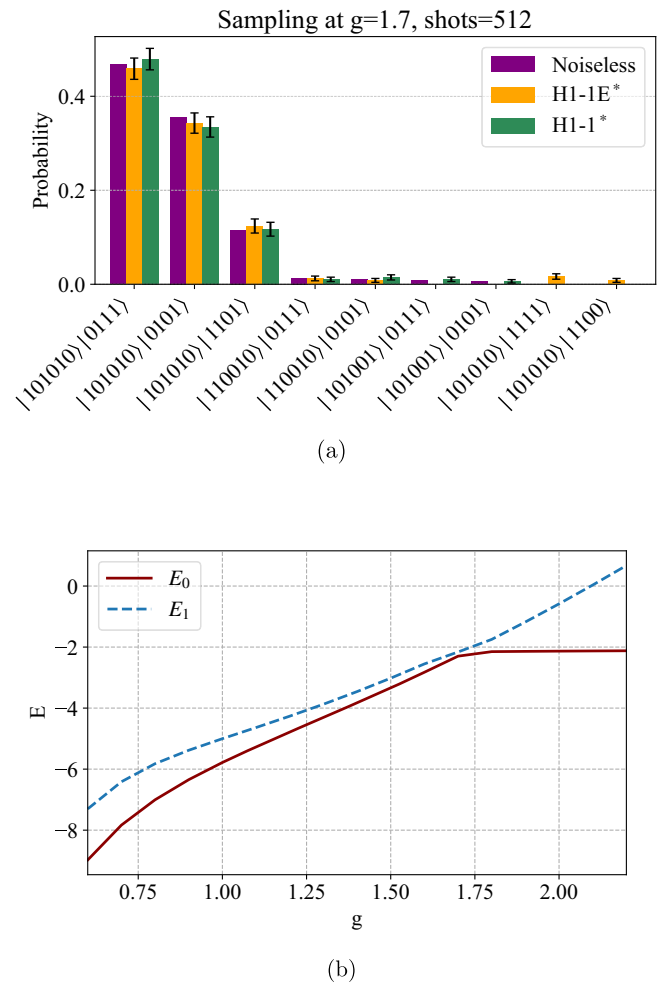


Fig. 6 | Ground state probabilities at coupling $g = 1.7$ and results of energy gap. **a** (bars from left to right) Noiseless results (state vector calculation with the optimal parameter from VQE), emulator H1-1E and real quantum hardware H1-1. The emulator and hardware results were performed in a single run with 512 shots. The data mitigated by excluding the unphysical bitstrings are indicated by (\dagger). The error bars on the probability are obtained by considering the shots to be drawn from a Bernoulli distribution. **b** Data with exact diagonalization for the ground state (E_0 , solid line) and first excited state (E_1 , dashed line) at different couplings g . The gap $E_1 - E_0$ closes when approaching $g \sim 1.7$.

points computed with H1-1E or H1-1 and the noiseless results at $g = 0.7, 1.1, 1.5$. The uncertainties are computed with Eq. (13). From Fig. 7, we can see that, generally, both the emulator and hardware results can reproduce the expected behavior. In the case of the smallest coupling, $g = 0.3$, we have a good agreement between the noiseless result and the result from H1-1E, and expect to reach a better understanding of the systematic errors if we consider multiple runs of the hardware experiment. For other couplings, we have good agreement on both the emulator and the hardware (blue circles). Lastly, we note that the last point $g = 1.9$ is only a variational bound on the expectation value, since it is obtained by sampling in the computational basis and considering only a subset of states for the calculation of the energy³⁹. For this reason we do not report the statistical error due to the shots.

4 × 3 lattice

This section studies the static potential for a larger 4×3 lattice, as depicted in Fig. 8a, where the static charges are placed at a distance $r = 3$ onto the two fermionic sites (n_x, n_y): $Q = 1 \mapsto (0, 1)$, $Q = -1 \mapsto (3, 1)$.

For this system we used a total of 24 qubits: 12 for the fermionic sites and 2·6 for the six dynamical gauge links (with truncation $l = 1$). We built the

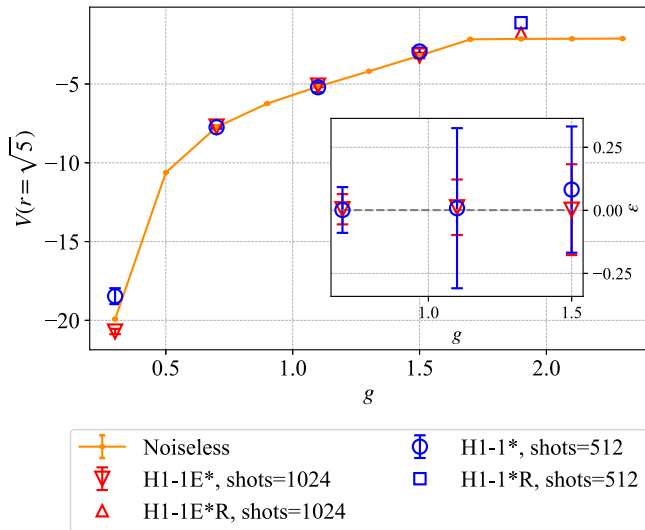


Fig. 7 | Static potential results with emulator H1-1E and quantum hardware H1-1. The orange curve represents the noiseless results (error bars smaller than the markers). For the results of the emulator (triangles) we used 1024 shots for each coupling, while for runs on H1-1 (circles and square) we used 512 shots. PMSV and SPAM mitigations are considered for the first four couplings $g = 0.3, 0.7, 1.1, 1.5$, (data indicated by $(^*)$). The uncertainties refer to the standard deviation, Eq. (13). The last data point, at $g = 1.9$ has been found via the basis sampling approach, selecting $R = 4$ dominant states, (data indicated by $(^R)$) and it is a variational bound on the energy. The inserted plot highlights the relative error ϵ between the data points computed with H1-1E or H1-1 and the noiseless results at $g = 0.7, 1.1, 1.5$.

quantum circuit, with a similar structure of the smaller lattice 3×2 , that is, by using the knowledge of the mutual information for the smaller system, we applied the entangling gates accordingly (“Supplementary Note 4: Variational quantum circuit for 4×3 lattice”). Table 2 shows the resources needed for this quantum circuit. Note that the CNOT depth for this system is more than doubled compared to the 3×2 lattice, and the raw number of CNOT operations is three times the one on the small system.

In Fig. 8b we illustrate the first attempt to compute the static potential with this larger system and a quantum variational approach. The uncertainties are computed with Eq. (13). The quantum variational results (triangles), performed with 10^4 shots and the NFT optimizer, are able to qualitatively reproduce the static potential curve (solid line and dots), when simulated without the presence of noise. We also measure the fidelity to be 65–95% for the couplings $g = 0.7, 1.1, 1.9$ respectively, suggesting that we have not reached convergence for some of them. In order to run a circuit with 24 qubits also on the H1-1E emulator and the H1-1 quantum computer (with up to 20 physical qubits), we employ the automatic qubit reuse compilation⁴¹ made possible by the mid-circuit measurement and reset capabilities of Quantinuum H-series devices and implemented in the TKET quantum compiler⁴². By measuring 9 qubits in the middle of the circuit executions and resetting them to be reused in the same circuit, we obtain an equivalent circuit that requires only 15 physical qubits and can therefore be used for our experiments on H1-1. The circuit with 15 qubits is rebased on the native gates of H-series and optimized: the total number of two-qubit R_{zz} gate operations is approximately 270 at all couplings, a major reduction compared to the resource in Table 2. Thus, by implementing this technique, we can sample from the state prepared by a larger circuit, but using only the limited resources available.

We study some of the interesting lattice configurations that arise in this larger 4×3 system. For example, at coupling $g = 0.7$, the most probable computational basis state is $|\psi_f\rangle \otimes |\psi_g\rangle = |\nu\rangle \otimes |\nu\rangle$, shown in panel (a) of Fig. 9, see also Section “Methods”. Here $|\nu\rangle$ is the vacuum, i.e. no dynamical charges on the sites and zero values for dynamical links. The second most

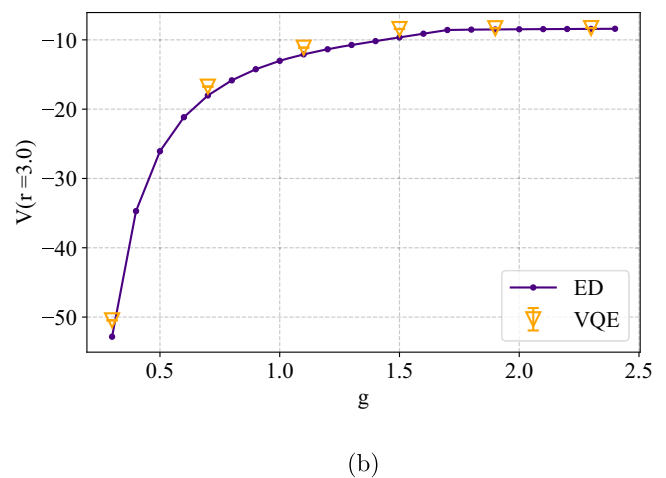
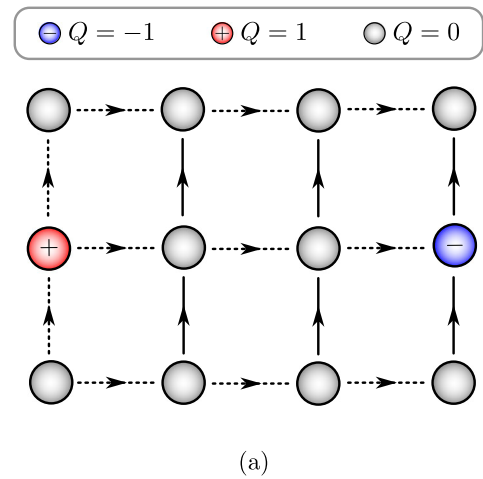


Fig. 8 | Lattice system 4×3 and variational quantum results (noiseless simulator). a Two static charges with values $Q = \pm 1$ are placed onto two sites (n_x, n_y) : $Q = 1 \mapsto (0, 1)$, $Q = -1 \mapsto (3, 1)$. The dashed arrows are the inactive gauge links after Gauss’s law is applied, solid arrows represent the link operators that remain dynamical. b Static potential at different coupling g at truncation $l = 1$ with Exact Diagonalization (ED) (solid line) and quantum variational results (triangles), performed with Nakanishi–Fujii–Todo (NFT) optimizer and 10^4 shots. A finite number of shots defines the error bars, which are smaller than the markers.

Table 2 | Resources required for the variational circuit for Gray encoding at different gauge fields truncation l

Resource estimation 4×3 OBC system				
l	# Qubits	# CNOTs	CNOT Depth	# Parameters
1	24	450	136	81
3	30	582	186	123
7	36	738	238	177

In a 4×3 Open Boundary Conditions (OBC) system with fermions, the six dynamical gauge fields and fermionic sites can be simulated with the specified total number of qubits. In particular, the number of qubits for the fermions is fixed to 12. Additionally, we quantify the total count of CNOT gates and the CNOT depth, representing the layers of CNOT gates in the circuit. The rightmost column displays the total number of parameters in the variational Ansatz.

probable state is $|\psi_f\rangle \otimes |\psi_g\rangle = |\nu\rangle \otimes |0001010101\rangle$ and it corresponds to the configuration illustrated in panel (b). The probability associated with these additional states having a snake-like pattern of the flux tube vanishes when going to stronger couplings and the straight flux tube (Fig. 9a)

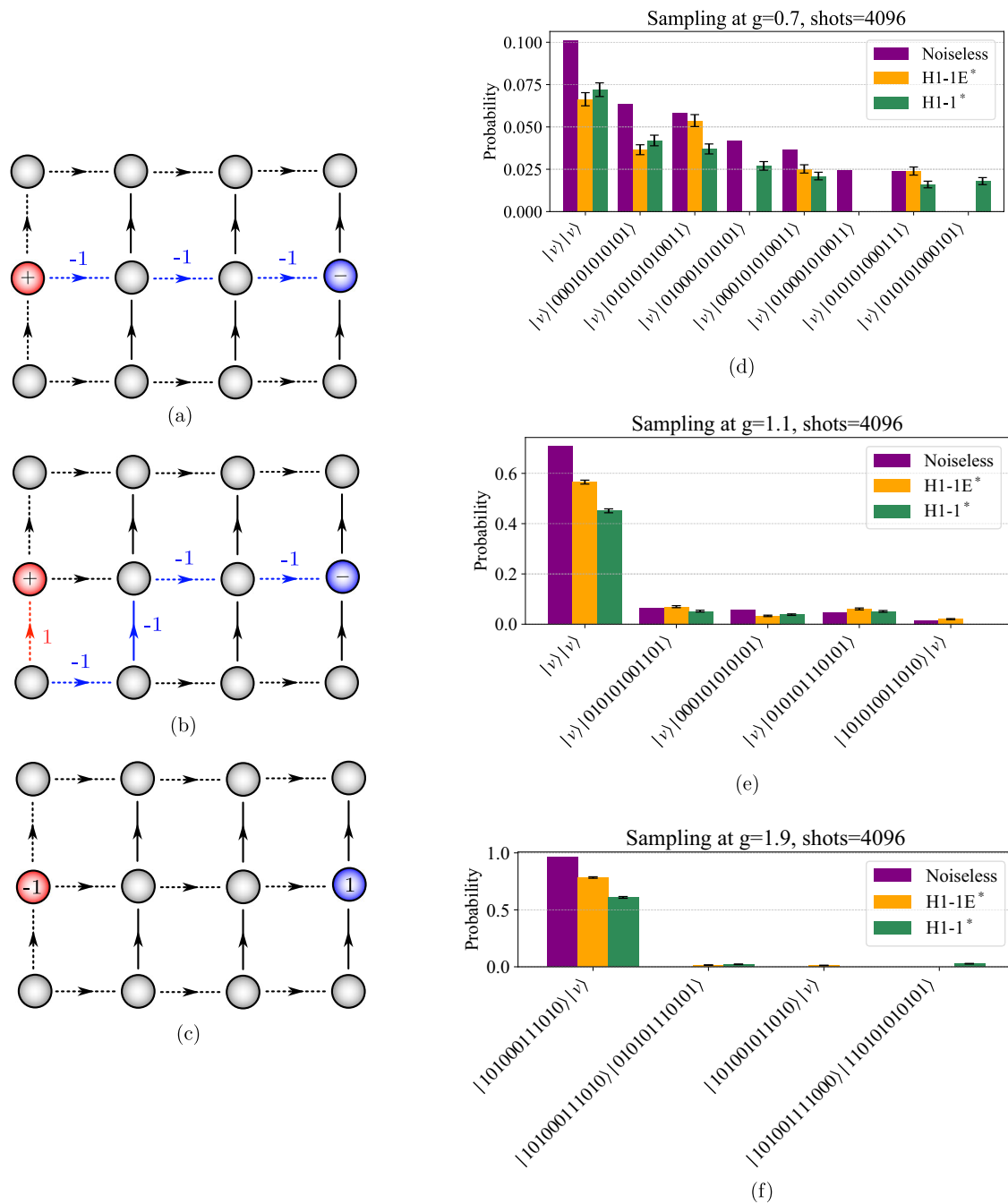


Fig. 9 | Ground state probabilities with reduced circuit at coupling $g = 0.7, 1.1, 1.9$. At small couplings, the electric string can propagate through the lattice. At stronger g , the dominant configuration becomes the straight string between the static charges, until it breaks and two dynamical charges form. On the x -axis of the plots (d–f), the bit strings are written as $|\Psi\rangle = |\psi_f\rangle \otimes |\psi_g\rangle$. **a** Represents the leftmost configuration $|\nu\rangle \otimes |\nu\rangle$ in (d) and (e), i.e. zero eigenvalues for the six dynamical gauge fields (solid arrows) and no dynamical charges on the sites. By applying Gauss' law, this translates into the lattice with a straight electric flux between the static charges. Static charges correspond to \pm symbols on the sites. The electric flux is depicted with blue/red arrows with a value of $-1/+1$. The inactive gauge links are depicted with dashed arrows. **b** Illustrates an example of a configuration which extends through external sites and corresponds to the second configuration from the left (d). **c** Illustrates the configuration at coupling $g = 1.9$ where the electric string is broken, and two dynamical charges are formed, represented with numerical values ± 1 on the sites, and forming pairs with the already existing static

charges on the same sites (\pm charge with $-1/+1$ dynamical one and $-1/+1$ charge with $1/-1$). In this figure we only write the values of the dynamical charges, keeping the colors on the sites for the static charges. **d** Noiseless results at coupling $g = 0.7$ (state vector calculation with the optimal parameter from VQE), emulator H1-1E and real quantum hardware H1-1. **e** Noiseless results at coupling $g = 1.1$ (state vector calculation with the optimal parameter from VQE), emulator H1-1E and real quantum hardware H1-1. The configuration with a larger probability corresponds to the lattice in (a). **f** Noiseless results at coupling $g = 1.9$ (state vector calculation with the optimal parameter from VQE), emulator H1-1E and real quantum hardware H1-1. The configuration with a larger probability corresponds to the lattice (c). In all the data, the emulator and hardware results were performed in a single run with 4096 shots. The data mitigated by excluding the unphysical bitstrings are indicated by $\hat{\cdot}$. In all plots, the error bars on the probability are obtained by considering the shots to be drawn from a Bernoulli distribution.

dominates. We see this at the stronger coupling $g = 1.1$ in Fig. 9e. At $g = 1.9$, on the other hand, we have the breaking of the electric string and the formation of mesons pairs, shown in Figs. 9c, f.

Discussion

In this paper we have performed a qualitative analysis of the static potential between two static charges, exploring the Coulomb, confinement and string breaking regimes where, by sampling over the states in the ground state energy, we determined the electric flux configurations and the probabilities of the contributing states. To this end, we developed a symmetry-preserving variational quantum circuit and employed a variational quantum algorithm to create the ground state of the Hamiltonian, corresponding to the static potential. Additionally, in the design of the Ansatz, we employed the mutual information between qubits, which led to a reduction of the depth of the quantum circuit. In order to explore the different regimes of the potential we used selected values of the coupling constant, corresponding to different physical distances.

We have focused our studies on a 3×2 lattice with open boundary conditions and demonstrated that results from quantum experiments on a trapped-ion emulator, H1-1E, and a real quantum device, H1-1, agreed with classical noiseless simulations for the static potential, obtained with the application of the mentioned quantum variational approach. The relevant electric flux configurations, which contribute to the quantum ground state in the different distance regimes of the static potential, were visualized by applying Gauss's law to sampled bitstrings. These results are qualitatively consistent with confinement and string-breaking behavior, gaining insights on the flux tube structure of the ground state.

We also considered experiments on a larger system, of 4×3 fermionic sites, with a 24 qubit variational circuit. An implementation on the 20 qubits of the H1-1 quantum device becomes possible with the reduction of the number of qubits from 24 to 15. In the current mutual-information adapted Ansatz, this was achieved by using mid-circuit measurements, resetting selected qubits and reusing them in the quantum computation.

Considering further hardware results with the largest Quantum ion-trap devices, a possibility is to study a 6×4 lattice, which requires up to a total of 54 qubits for the quantum computation, thus suitable for the H2 device⁴³. This exciting outlook to go to larger system sizes in the future offers new possibilities. First, it will allow to study the static potential as a function of the distance in lattice units, which provides the opportunity to fit the anticipated analytical form of the potential and extract the values of the coupling, the string tension and the distance, where string breaking occurs, on a quantitative level. Second, it will become possible to determine the properties of the confining string, such as its width and the fluctuations, quantitatively. By combining these Hamiltonian calculations with Monte Carlo simulations, which will provide a physical value of the lattice spacing⁴⁴, we can eventually give results in physical units, which could be relevant for experiments described by $(2 + 1)$ dimensional QED. However, we believe that to achieve this goal, further improvements of quantum circuit design as well as advances in quantum hardware are needed. For example, with the here used standard implementation of VQE, it would become infeasible to train the variational parameters of the Ansatz, whose number will also scale with the size of the system: this may be circumvented by other scalable variational approaches, such as SC-ADAPT-VQE⁴⁵, or by adiabatic evolution based on a Trotterized Hamiltonian with reduced Trotter errors⁴⁶. However, these methods need to be further tested in the future. We also mention that there are corrections to the linear potential, originating from fluctuations of the electric flux string, see refs. 47–50 and a recent work ref. 51. It would be very interesting to determine this correction within our setup by considering different lattices geometries allowing larger separations of the static charges. We remark that recently also a Hamiltonian formulation of Maxwell-Chern-Simons theory has been developed for compact $U(1)$ gauge theory on the lattice⁵², which combines confinement and topology and opens new avenues to look at confinement properties in a non-perturbative fashion.

Methods

This work will consider a variational quantum approach to study the static potential. A parameterized quantum circuit is used to efficiently prepare the ground state of the Hamiltonian at various values of the coupling g and the expectation value of the Hamiltonian itself will allow us to map out the static potential function $V(r)$. To employ this method we prepare a quantum circuit with parameterized gates as our ground state Ansatz. The main property we endow on our Ansatz is the ability to explore only the physical Hilbert space, thus being more efficient in representing the allowed quantum states of the theory. In particular, we restrict the space of states to the truncated Hilbert space for the gauge fields and to the fermionic sector with zero total charge. This section describes how we encode the gauge and fermionic degrees of freedom on the lattice into qubits and the set of quantum gates utilized in the variational algorithm. The python code used in this paper to build the $(2 + 1)$ -d QED lattice Hamiltonian and the parameterized quantum circuit are available⁵³.

Encoding of gauge fields

For the implementation on a quantum circuit it is advantageous to employ a suitable encoding that accurately represents the physical values of gauge fields. Examples can be the *linear encoding*⁵⁴, where gauge physical states are mapped onto $2l + 1$ qubits, or the *logarithm encoding*³¹. With the latter formulation, the minimum number of qubits required for each gauge variable is $q_{\min} = \lceil \log_2(2l + 1) \rceil$. In this work we consider the *Gray encoding*⁵⁵ to represent the physical values of the gauge fields in a quantum simulation. With this approach, the encoded gauge fields are chosen in such a way that the difference in the bit string representation of the states, when applying lowering and raising operators, is just a single bit. In addition, since our objective is to do a qualitative analysis, in this project we will mainly consider the truncation $l = 1$, with additional details about other truncation values in “Supplementary Note 3: Truncation and Gauss's law dependence”. With $l = 1$ we have the following states,

$$|-1\rangle_{\text{ph}} \mapsto |00\rangle, \tag{14a}$$

$$|0\rangle_{\text{ph}} \mapsto |01\rangle, \tag{14b}$$

$$|1\rangle_{\text{ph}} \mapsto |11\rangle. \tag{14c}$$

Here, and in the rest of the paper, we follow the *right-left* ($|\dots q_2 q_1 q_0\rangle$), *top-bottom* ordering of the qubits.

The circuit, depicted in Fig. 10a, can be understood as follows:

- Beginning with the state $|00\rangle$, setting both parameters θ_1 and θ_2 to zero enables the representation of the physical state $|-1\rangle_{\text{ph}}$, Eq. (14a).
- When a non-zero value is assigned to θ_1 , the state transitions to $|01\rangle$, representing the vacuum state (Eq. (14b)), with a certain probability.
- A full rotation occurs when $\theta_1 = \pi$, ensuring that the second state is achieved with a probability of 1.0.
- After this, the second controlled gate is activated only if the first qubit is $|1\rangle$, allowing the exploration of $|11\rangle$ (Eq. (14c)) and excluding $|10\rangle$.

Encoding of fermionic fields

The fermionic degrees of freedom at site \mathbf{n} can be mapped to spins using a Jordan–Wigner transformation⁵⁶,

$$\hat{\phi}_{\mathbf{n}} = \left[\prod_{\mathbf{k} < \mathbf{n}} (-i\sigma_{\mathbf{k}}^z) \right] \sigma_{\mathbf{n}}^+, \tag{15a}$$

$$\hat{\phi}_{\mathbf{n}}^\dagger = \left[\prod_{\mathbf{k} < \mathbf{n}} (i\sigma_{\mathbf{k}}^z) \right] \sigma_{\mathbf{n}}^-, \tag{15b}$$

where $\sigma_{\mathbf{n}}^\pm = \frac{\sigma_{\mathbf{n}}^x \pm i\sigma_{\mathbf{n}}^y}{2}$ ($\sigma_{\mathbf{n}}^x, \sigma_{\mathbf{n}}^y, \sigma_{\mathbf{n}}^z$ are Pauli matrices, and $I_{\mathbf{n}}$ is the identity matrix, acting on the spin at site \mathbf{n}). The relation between site coordinates

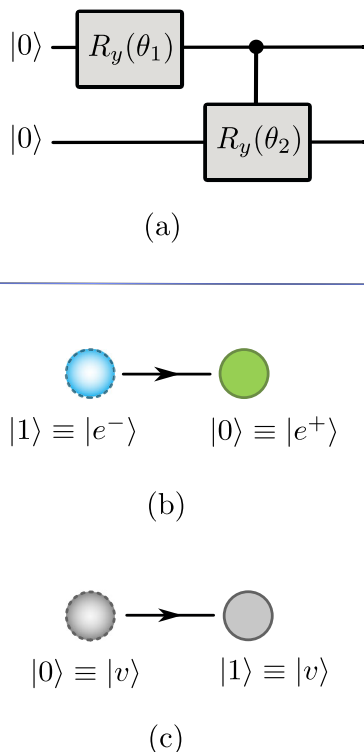


Fig. 10 | Variational circuit for Gray encoding with $l = 1$ and fermionic sites configurations. **a** Vacuum state is $|01\rangle$, and state $|10\rangle$ is excluded. If the state on even sites (dotted circles) is $|1\rangle$ **(b)** $(|0\rangle, \text{c})$, there is a particle, e^- , (vacuum, v) on that site. In the case of odd sites (solid circles) if $|0\rangle$ **(b)** $(|1\rangle, \text{c})$, we have an antiparticle, e^+ , (vacuum, v).

$\mathbf{k} < \mathbf{n}$ is defined to satisfy the fermionic anticommutation relations. For example, in the 3×2 OBC system, we use the chain $(0, 0) \rightarrow (1, 0) \rightarrow (2, 0) \rightarrow (2, 1) \rightarrow (1, 1) \rightarrow (0, 1)$. The dynamical charges, Eq. (7), can be written as

$$\hat{q}_{\mathbf{n}} \mapsto \begin{cases} \frac{I_{\mathbf{n}} - \sigma_{\mathbf{n}}^z}{2} & \text{if } \mathbf{n} \text{ even,} \\ -\frac{I_{\mathbf{n}} + \sigma_{\mathbf{n}}^z}{2} & \text{if } \mathbf{n} \text{ odd.} \end{cases} \quad (16)$$

The mass term Eq. (2c) in the Hamiltonian identifies the Dirac vacuum with the state where the odd fermionic sites are occupied, and creating a particle at an even site is equivalent to creating a charged $q = 1$ fermion in the Dirac vacuum. Destroying a particle at odd sites is thus equivalent to creating an antifermion with charge $q = -1$. With the vacuum state on the fermionic sites represented as $|..1010\rangle$, we can summarize the configurations in Table 3 (the first site is even $\mathbf{n} = (n_x, n_y) = (0, 0)$).

These configurations are visualized also in Figs. 10b, c, where we have in panel (b) the case with a particle, e^- , on the even site and an antiparticle, e^+ , on the odd site, corresponding to charges $q = 1, -1$, respectively. Panel (c) shows the situation with vacuum states, v , both on even/odd sites.

We now define a quantum circuit that excludes the states with non-zero total charge, i.e. that do not have the same number of ‘0’ and ‘1’. This can be achieved with a set of parameterized i SWAP $_{j,k}(\theta) = e^{-i\theta(\sigma_j^x \sigma_k^x + \sigma_j^y \sigma_k^y)}$ gates, where j and k are the qubits on which the gate acts and θ an angle parameter⁵⁴. They can be realized with a combination of parameterized rotational gates $R_{xx}(\theta) = e^{-i\theta\sigma_x}$ and $R_{yy}(\theta) = e^{-i\theta\sigma_y}$ on two qubits. The action of the i SWAP gate is swapping the values of two qubits, i.e. if we start from a state $|10\rangle$, $R_{xx}(\theta/2)R_{yy}(\theta/2)|10\rangle$ with $\theta = \frac{\pi}{2}$ will give us $|01\rangle$. With these gates, we can explore the fermionic states in the Hilbert space with zero total charge. If we choose the NFT optimizer³⁷, we need to satisfy a set of

Table 3 | Particle configurations on a 2D lattice

	$ 0\rangle$	$ 1\rangle$
$n_x + n_y = \text{even}$	$q = 0$ vacuum	$q = 1$ fermion
$n_x + n_y = \text{odd}$	$q = -1$ antifermion	$q = 0$ vacuum

Sites $\mathbf{n} = (n_x, n_y)$ are considered even/odd from the sum of the two coordinates n_x, n_y on the lattice. The vacuum state is $|..1010\rangle$ and the configuration with particles/antiparticles at every site is $|..0101\rangle$. (Note that these configurations depend on the choice of the Jordan–Wigner transformation).

requirements, one being that the gates in the variational circuits must be of the form $R(\theta) = e^{-i\theta A}$ with $A^2 = I$. However, $[\frac{1}{2}(\sigma_j^x \sigma_k^x + \sigma_j^y \sigma_k^y)]^2 \neq I$. To solve this issue, we can extend the gate to $\frac{1}{2}(\sigma_j^x \sigma_k^x + \sigma_j^y \sigma_k^y + \sigma_j^z \sigma_k^z + I_j I_k)$, which satisfies the condition. Note that we can discard the identity and we only need to implement the $R_{zz}(\theta/2) = e^{-i\frac{\theta}{4}\sigma_z \sigma_z}$.

The states of a generic system will be written as the tensor product of gauge fields states and fermionic states: $|\Psi\rangle = |\psi_f\rangle \otimes |\psi_g\rangle$. With this ordering we can read the quantum variational solutions and identify the corresponding configuration of gauge and fermionic degrees of freedom. For example, the vacuum state for a 3×2 system, will correspond to $|01\rangle$ states for each gauge field (truncation $l = 1$) and $|101010\rangle$ for the six fermionic sites. Combining them, we get that the vacuum state is $|\nu\rangle = |101010\rangle \otimes |0101\rangle$.

Quantum hardware

The optimal quantum circuits, resulting from the variational quantum parameters, that prepare the ground state at various couplings are run on Quantum H-series System Model H1-1, both in emulation and in real hardware²⁴. The quantum job submission workflow is supported by the Quantum Nexus cloud platform⁵⁷.

The quantum device we utilize is based on the QCCD architecture⁵⁸ and it shuttles Ytterbium-171 ions along a linear trap, with the qubit information stored in the ion’s atomic hyperfine states. Each Ytterbium ion is paired in a crystal with a Barium ion used for sympathetic laser cooling. A total of up to 20 qubits can be manipulated across 5 parallel gate zones, realizing an effective all-to-all connectivity between qubits that is advantageous for the circuits representing our Ansatz. The H1-1 device can be emulated with an accurate physical noise model using the H1-1E emulator^{59,60}. We use the emulator in its statevector configuration.

Noise mitigation

In the present paper we employ two types of noise mitigation techniques to post-process the resulting shot counts and expectation values. The first one is the Partition Measurement Symmetry Verification (PMSV)⁶¹ method, which uses global symmetries of the Hamiltonian to validate measurements, before combining shots to compute expectation values across multiple circuits. Another approach involves mitigating state preparation and measurement (SPAM) noise⁶². With SPAM, the noise-induced errors are considered only to occur during the state preparation and measurement steps. This method uses the density matrix to first get the noise profile of the device when it comes to readout operations: this is achieved with the submission of a calibration circuit. Then, it computes the inverse of this matrix, suppressing the errors caused by the noise channels in the readout. Both PMSV and SPAM are implemented in the quantum computational software InQuanto⁴⁰.

Moreover, since we are only interested in the zero-charge sector for the fermionic sites and the truncated Hilbert space for the gauge fields, we apply a simple symmetry-based error detection post-processing step during the sampling in the computational basis. We exclude the shots whose bitstrings do not satisfy the fermionic symmetry constraints and that fall outside of the physical Hilbert space of the gauge links. After the selection of the physical bitstrings, the probability distribution is computed on the renormalized

counts. We will consider this post-selection for the sampling analysis, while we will use PMSV and SPAM to compute the Hamiltonian expectation values.

Data availability

The data that support the findings of this study are available from the corresponding author upon request.

Code availability

A python code implementation for the truncation scheme as well as quantum circuit construction is available at ref. 53.

Received: 31 January 2025; Accepted: 12 December 2025;

Published online: 30 January 2026

References

- Wilson, K. G. Confinement of Quarks. *Phys. Rev. D.* **10**, 2445–2459 (1974).
- Rothe, H. J. *Lattice Gauge Theories: An Introduction* (World Scientific Publishing Company, 2012).
- Gattringer, C. & Lang, C. *Quantum Chromodynamics on the Lattice: An Introductory Presentation*, vol. 788 (Springer Science & Business Media, 2009).
- Gross, F. et al. 50 years of quantum chromodynamics. *Eur. Phys. J. C.* **83**, 1125 (2023).
- Polyakov, A. M. Quark confinement and topology of gauge groups. *Nucl. Phys. B* **120**, 429–458 (1977).
- Wen, X.-G. *Quantum Field Theory of Many-body Systems*. (Oxford University Press, New York, NY, 2004).
- Knechtli, F. & Sommer, R. String breaking as a mixing phenomenon in the SU(2) Higgs model. *Nucl. Phys. B* **590**, 309–328 (2000).
- Philipsen, O. & Wittig, H. String breaking in nonAbelian gauge theories with fundamental matter fields. *Phys. Rev. Lett.* **81**, 4056–4059 (1998).
- Bali, G. S. QCD forces and heavy quark bound states. *Phys. Rept.* **343**, 1–136 (2001).
- Loan, M., Brunner, M., Sloggett, C. & Hamer, C. Path integral Monte Carlo approach to the U(1) lattice gauge theory in 2+1 dimensions. *Phys. Rev. D.* **68**, 034504 (2003).
- Bender, J., Emonts, P., Zohar, E. & Cirac, J. I. Real-time dynamics in 2+1d compact QED using complex periodic gaussian states. *Phys. Rev. Res.* **2**, 043145 (2020).
- Banuls, M. C. et al. Simulating lattice gauge theories within quantum technologies. *Eur. Phys. J. D.* **74**, 1–42 (2020).
- Bauer, C. W. et al. Quantum simulation for high-energy physics. *PRX Quantum* **4**, 027001 (2023).
- Di Meglio, A. et al. Quantum computing for high-energy physics: state of the art and challenges. *PRX Quantum* **5**, 037001 (2024).
- Funcke, L., Hartung, T., Jansen, K. & Kühn, S. Review on quantum computing for lattice field theory. *PoS LATTICE2022*, 228 (2023).
- Banerjee, D. et al. Atomic quantum simulation of dynamical gauge fields coupled to fermionic matter: from string breaking to evolution after a quench. *Phys. Rev. Lett.* **109**, 175302 (2012).
- Wiese, U.-J. Ultracold quantum gases and lattice systems: quantum simulation of lattice gauge theories. *Ann. der Phys.* **525**, 777–796 (2013).
- Zohar, E., Cirac, J. I. & Reznik, B. Quantum simulations of lattice gauge theories using ultracold atoms in optical lattices. *Rep. Prog. Phys.* **79**, 014401 (2015).
- Magnifico, G., Felser, T., Silvi, P. & Montangero, S. Lattice quantum electrodynamics in (3+1)-dimensions at finite density with tensor networks. *Nat. Commun.* **12**, 3600 (2021).
- Zohar, E. & Reznik, B. Confinement and lattice quantum-electrodynamic electric flux tubes simulated with ultracold atoms. *Phys. Rev. Lett.* **107**, 275301 (2011).
- Cochran, T. A. et al. Visualizing dynamics of charges and strings in (2+1)D lattice gauge theories. *Nature* **642**, 1–6 (2025).
- De, A. et al. Observation of string-breaking dynamics in a quantum simulator. Preprint at <https://arxiv.org/abs/2410.13815> (2024).
- González-Cuadra, D. et al. Observation of string breaking on a (2+1)D Rydberg quantum simulator. *Nature* **642**, 1–6 (2025).
- Quantinuum H1-1. <https://www.quantinuum.com/products-solutions/system-model-h1-series> (2024).
- Kogut, J. & Susskind, L. Hamiltonian formulation of wilson's lattice gauge theories. *Phys. Rev. D.* **11**, 395–408 (1975).
- Robson, D. & Webber, D. Gauge theories on a small lattice. *Z. Phys. C. Part. Fields* **7**, 53–60 (1980).
- Ligterink, N., Walet, N. & Bishop, R. A many-body treatment of hamiltonian lattice gauge theory. *Nucl. Phys. A Nucl. Hadronic Phys.* **663**, 983c–986c (2000).
- Nielsen, H. B. & Ninomiya, M. No go theorem for regularizing chiral fermions. *Phys. Lett. B* **105**, 219–223 (1981).
- Susskind, L. Lattice fermions. *Phys. Rev. D.* **16**, 3031–3039 (1977).
- Haase, J. F. et al. A resource efficient approach for quantum and classical simulations of gauge theories in particle physics. *Quantum* **5**, 393 (2021).
- Mathis, S. V., Mazzola, G. & Tavernelli, I. Toward scalable simulations of lattice gauge theories on quantum computers. *Phys. Rev. D.* **102**, 094501 (2020).
- Chandrasekharan, S. & Wiese, U.-J. Quantum link models: a discrete approach to gauge theories. *Nucl. Phys. B* **492**, 455–471 (1997).
- Hashizume, T., Halimeh, J., Hauke, P. & Banerjee, D. Ground-state phase diagram of quantum link electrodynamics in (2+1)-d. *SciPost Phys.* **13**, <https://doi.org/10.21468/SciPostPhys.13.2.017> (2022).
- Notarnicola, S. et al. Discrete abelian gauge theories for quantum simulations of qed. *J. Phys. A Math. Theor.* **48**, 30FT01 (2015).
- Meth, M. et al. Simulating 2d lattice gauge theories on a qudit quantum computer. Preprint at <https://arxiv.org/abs/2310.12110> (2023).
- Peruzzo, A. et al. A variational eigenvalue solver on a photonic quantum processor. *Nat. Commun.* **5**, 4213 (2014).
- Nakanishi, K. M., Fujii, K. & Todo, S. Sequential minimal optimization for quantum-classical hybrid algorithms. *Phys. Rev. Res.* **2**, 043158 (2020).
- Ostaszewski, M., Grant, E. & Benedetti, M. Structure optimization for parameterized quantum circuits. *Quantum* **5**, 391 (2021).
- Kohda, M. et al. Quantum expectation-value estimation by computational basis sampling. *Phys. Rev. Res.* **4**, 033173 (2022).
- Tranter, A. et al. InQuanto: quantum computational chemistry. <https://www.quantinuum.com/products-solutions/inquanto> (2022).
- DeCross, M., Chertkov, E., Kohagen, M. & Foss-Feig, M. Qubit-reuse compilation with mid-circuit measurement and reset. *Phys. Rev. X* **13**, 041057 (2023).
- Sivarajah, S. et al. t|ket>: a retargetable compiler for NISQ devices. *Quantum Sci. Technol.* **6**, 014003 (2020).
- Quantinuum H2-1. <https://www.quantinuum.com/products-solutions/system-model-h2-series> (2024).
- Crippa, A. et al. Towards determining the (2+1)-dimensional Quantum Electrodynamics running coupling with Monte Carlo and quantum computing methods. *Commun. Phys.* **8**, 367 (2025).
- Farrell, R. C., Illa, M., Ciavarella, A. N. & Savage, M. J. Scalable Circuits for Preparing Ground States on Digital Quantum Computers: The Schwinger Model Vacuum on 100 Qubits. *PRX Quantum* **5**, 020315 (2024).
- Granet, E., Ghanem, K. & Dreyer, H. Practicality of a quantum adiabatic algorithm for chemistry applications. *Phys. Rev. A.* **111**, 022428 (2025).
- Luescher, M. Symmetry-breaking aspects of the roughening transition in gauge theories. *Nucl. Phys. B* **180**, 317–329 (1981).
- Lüscher, M. & Weisz, P. Quark confinement and the bosonic string. *J. High. Energy Phys.* **2002**, 049 (2002).

49. Nogueira, F. S. & Kleinert, H. Quantum electrodynamics in 2+ 1 dimensions, confinement, and the stability of u (1) spin liquids. *Phys. Rev. Lett.* **95**, 176406 (2005).
50. Chagdaa, S., Galsandorj, E., Laermann, E. & Purev, B. Width and string tension of the flux tube in su (2) lattice gauge theory at high temperature. *J. Phys. G: Nucl. Part. Phys.* **45**, 025002 (2017).
51. Caselle, M., Cellini, E. & Nada, A. Numerical determination of the width and shape of the effective string using stochastic normalizing flows. *J. High Energ. Phys.* **2025**, 1–30 (2025).
52. Peng, C. et al. Hamiltonian lattice formulation of compact Maxwell-Chern-Simons theory. Preprint at <https://arxiv.org/abs/2407.20225> (2024).
53. Crippa, A. QED_Hamiltonian/v0.0.2, https://github.com/ariannacrippa/QC_lattice_H (2024).
54. Paulson, D. et al. Simulating 2d effects in lattice gauge theories on a quantum computer. *PRX Quantum* **2**, 030334 (2021).
55. Di Matteo, O. et al. Improving hamiltonian encodings with the gray code. *Phys. Rev. A* **103**, 042405 (2021).
56. Jordan, P. & Wigner, E. *Über das paulische äquivalenzverbot* (Springer, 1993).
57. Quantinuum nexus, <https://nexus.quantinuum.com/> (2024).
58. Pino, J. M. et al. Demonstration of the trapped-ion quantum CCD computer architecture. *Nature* **592**, 209 (2021).
59. Ryan-Anderson, C. Pecos: performance estimator of codes on surfaces. <https://github.com/PECOS-packages/PECOS> (2018).
60. Ryan-Anderson, C. et al. Realization of real-time fault-tolerant quantum error correction. *Phys. Rev. X* **11**, 041058 (2021).
61. Yamamoto, K., Manrique, D. Z., Khan, I. T., Sawada, H. & Ramo, D. M. Quantum hardware calculations of periodic systems with partition-measurement symmetry verification: Simplified models of hydrogen chain and iron crystals. *Phys. Rev. Res.* **4**, <https://doi.org/10.1103/PhysRevResearch.4.033110> (2022).
62. Jackson, C. & van Enk, S. J. Detecting correlated errors in state-preparation-and-measurement tomography. *Phys. Rev. A* **92**, 042312 (2015).

Acknowledgements

We acknowledge Henrik Dreyer and David Zsolt Manrique for a careful review of the manuscript, and Irfan Khan for discussions on the qubit reuse automatic compilation. We thank the entire Quantinuum NEXUS team. We thank Davide Materia for sharing his work on the employment of the mutual information in quantum chemistry. We are grateful to Enrique Rico Ortega, Francesco Di Marcantonio and Maria Cristina Diamantini for fruitful discussions on the topic. This work is supported with funds from the Ministry of Science, Research and Culture of the State of Brandenburg within the Centre for Quantum Technologies and Applications (CQTA). A.C. is supported in part by the Helmholtz Association Innopool Project Variational Quantum Computer Simulations (VQCS). This work is funded by the European Union's Horizon Europe Frame-work Programme (HORIZON) under the ERA Chair scheme with grant agreement no. 101087126.

Author contributions

A. Crippa is the corresponding author of this manuscript. A. Crippa developed the quantum circuits and carried out the calculations in the Hamiltonian formalism with exact diagonalization, variational quantum computing approach and on quantum hardware. K. Jansen supervised the project and contributed to discussions of the results. E. Rinaldi applied the necessary transpilation and error mitigation techniques to run on the ion trap device and supervised the quantum hardware runs. All authors contributed to the writing of the manuscript.

Funding

Open Access funding enabled and organized by Projekt DEAL.

Competing interests

The authors declare no competing interests.

Additional information

Supplementary information The online version contains supplementary material available at <https://doi.org/10.1038/s42005-025-02465-8>.

Correspondence and requests for materials should be addressed to Arianna Crippa.

Peer review information *Communications Physics* thanks Or Katz and the other, anonymous, reviewer(s) for their contribution to the peer review of this work.

Reprints and permissions information is available at <http://www.nature.com/reprints>

Publisher's note Springer Nature remains neutral with regard to jurisdictional claims in published maps and institutional affiliations.

Open Access This article is licensed under a Creative Commons Attribution 4.0 International License, which permits use, sharing, adaptation, distribution and reproduction in any medium or format, as long as you give appropriate credit to the original author(s) and the source, provide a link to the Creative Commons licence, and indicate if changes were made. The images or other third party material in this article are included in the article's Creative Commons licence, unless indicated otherwise in a credit line to the material. If material is not included in the article's Creative Commons licence and your intended use is not permitted by statutory regulation or exceeds the permitted use, you will need to obtain permission directly from the copyright holder. To view a copy of this licence, visit <http://creativecommons.org/licenses/by/4.0/>.

© The Author(s) 2026